Electronic Supplementary Material (ESI) for Energy & Environmental Science.

Supplementary Information

High-permeance polymer-functionalized single-layer graphene membranes that surpass the postcombustion carbon capture target

Guangwei He[1], Shiqi Huang[1], Luis Francisco Villalobos[1], Jing Zhao[1], Mounir Mensi[2], Emad Oveisi[3], Mojtaba Rezaei[1], Kumar Varoon Agrawal[1]*

[1]Laboratory of Advanced Separations (LAS), École Polytechnique Fédérale de Lausanne (EPFL), Sion, Switzerland

[2]Institute of Chemical Sciences and Engineering (ISIC), EPFL, Sion, Switzerland

[3]Interdisciplinary Centre for Electron Microscopy (CIME), EPFL, Lausanne, Switzerland

E-mail: kumar.agrawal@epfl.ch

Materials and characterization

Synthesis of single-layer graphene. Single-layer graphene was synthesized by the low-pressure CVD of methane on a catalytic copper foil (25 µm, 99.98% purity, Sigma-Aldrich).[1,2] Briefly, the copper foil was annealed at 1000 ºC in a CO_2 atmosphere for 30 min to get rid of the organic contaminations.[3] Subsequently, the CO_2 flow was switched off and a H_2 flow (8 mL/min) was introduced to anneal the copper. Following this, CH_4 (24 mL/min) flow was introduced for 30 min at a total pressure of 460 mTorr to crystallize the single-layer graphene film.

Synthesis of ONG. An O_2 plasma was carried out to introduce nanopores in graphene (NG). For this, a piece of as-synthesized CVD graphene on the copper foil was placed in a plasma generator (MTI, EQ-PCE-3, 13.56 Mhz, 17 W). Subsequently, the chamber was evacuated to 50 mTorr pressure while maintaining a flow of O_2. After pressure stabilization, the plasma was generated for 2-8 s to etch the graphene lattice. ONG was synthesized by placing NG in an ozone atmosphere (7 wt% O_3 in O_2) generated by an ozone generator (Absolute Ozone® Atlas 30) for 20 min at room temperature.

Synthesis of PONG. PONG was prepared by spin-coating a dilute aqueous solution of CO_2-philic polymer on ONG. Aqueous solutions of branched PEI (average MW of 25000 g/mol, 10 mg/ml in water) or PEGBA (average MW of 1000 g/mol, 20 mg/ml) were used as the coating solutions. For coating, the solution was first spread on a stationary ONG. After 5 min, ONG was subjected to spinning, and 1 mL of the coating solution was added dropwise within 10 s. The spin-coating was carried out at 1000 rpm for 60 s, and then 3000 rpm for 60 s.

Reinforcement of PONG with PTMSP. A thin PTMSP film was coated onto the top of PONG by spin-coating to mechanically reinforce the PONG film, in order to prevent the PONG film from cracking during the transfer step. For this, a 1.25 wt% of PTMSP solution in toluene was spread on the PONG film, followed by spinning at 1000 rpm for 30 s, and then 2000 rpm for 30 s. The resulting film was dried in ambient conditions for 12 h, and then in a vacuum oven for 12 h at room temperature.

Synthesis of the SPONG membranes. The copper foil from the CVD step, acting as a substrate to the PTMSP-reinforced PONG film, was removed by chemical etching. This was carried out by placing the films on a $FeCl_3$ bath (1 M in water) for 30 min, which can chemically remove the copper foil. Then, the underside of the floating PONG film was rinsed with 0.1 M HCl solution for 1 h. The resulting film was floated on deionized water for 1 h to remove the copper residues. Following this, the film was floated on an aqueous solution of PEGDE (average MW of 500 g/mol, 2 mg/mL in water) for 24 h, to swell the PEI (or PEGBA) layer with PEGDE. Finally, the resulting SPONG film was scooped up using a porous tungsten support.[1] Briefly, the support had a porous area of 1 mm^2 consisting of an array of laser-drilled 5-µm-diameter pores. Post-transfer, the remaining PEGDE solution on the surface of the film was carefully removed by a blotting paper. The SPONG films were dried in a vacuum oven for 12 h at room temperature.

Characterization.

The Raman characterization was carried out using a Renishaw micro-Raman spectroscope equipped with a 457 nm excitation laser and a 50x objective. At least 10 spectra were obtained using the mapping method to analyze each sample. The I_D/I_G, and I_{2D}/I_G ratios were calculated by subtracting the background and using a curve-fitting tool in MATLAB. Measurements were carried out both before and after annealing the NG samples in an Ar/H_2 atmosphere at 300 °C for 2h.

Aberration-corrected (Cs) HRTEM was performed using a double-corrected Titan Themis 60-300 (FEI) equipped with a Wein-type monochromator. An 80 keV incident electron beam was used for all experiments to reduce the electron radiation damage. The incident electron beam was monochromated ("rainbow" mode illumination) to reduce the effects of chromatic aberration, and a negative Cs of ~15–20 μm and slight over focus were used to give a "bright atom" contrast in the images. The TEM samples were prepared by transferring a carbon-film coated graphene (Supplementary Note IV) onto a 1000-mesh gold TEM grid. The resulting HRTEM images were post-treated by a combination of Bandpass and Gaussian filters to reduce noise and improve contrast. Statistical summary of the porosity was based on a survey area over 10000 nm^2. The pore-density was calculated by sampling nanopores from a large area with the sample size greater than 10000 nm^2. The area of the pore was determined using the ImageJ software. The pore-diameter was calculated by assuming a circular pore with the same area.

The XPS analysis was performed on a VersaProbe II (Physical Electronics) using the monochromated Kα line of an aluminum X-ray source (1486.6 eV). The samples were electrically insulated from the sample stage and charge neutralization was used during the measurements performed at a low pass energy. The C1s line of the graphene-based samples was centered at 284 eV, which corresponds to the binding energy of sp^2 C-C bound. The exact C-N binding energy (~285.5 eV) was extracted from the position of the C1s line of the PEI reference sample. Peak fitting of the different components of the C1s peak was performed with Voigt functions after a Shirley background was subtracted. Four components with the following binding energies were fitted: C-C sp^2: 284.0 eV, C-C sp^3: 284.8 eV, C-O/C-N: 285.5 eV, C=O: 287.8 eV. For XPS, the PEI- or PEGBA-functionalized ONG were rinsed with water for 10 min to remove the excess polymers. The PEI reference sample was prepared by spin-coating a 10 mg/mL aqueous solution on a copper foil.

FEI Teneo SEM was used to observe the surface or cross-sectional morphologies of the as-synthesized films using an operating voltage of 1-5 kV and a working distance of 2.5 - 6.0 mm. The chemical composition was detected by an EDS detector (XFlash Silicon drift detector). No conductive coating was applied for observing the surface morphologies. For imaging the cross-sections, as-prepared cross-sections were coated with a 10-nm-thick iridium layer. Over three cross-sectional samples were imaged to ensure reliable measurement of the film thickness.

AFM measurements were carried out using a Nanoscope IIIa (Veeco, Santa Barabara, CA, USA), operating in the tapping-mode with the Nanosensors PPP-NCSTR probes. The topographic maps were flattened before the calculation of surface roughness and the height distribution histogram. To prepare PONG samples on Si wafer for AFM, graphene was transferred to a Si wafer by the conventional poly(methyl methacrylate) (PMMA) based wet-transfer technique[4]. Post-transfer, PMMA was removed by an acetone wash and a heat-treatment at 400 ºC for 2 h in an Ar/H_2 atmosphere. Subsequently, plasma treatment for 6 s, ozone treatment for 20 min, and spin-coating of PEI or PEGBA was carried out successively, using the same protocol as above, to obtain the PONG films.

The single-gas and mixture gas permeation measurements were carried out in a homemade permeation cell (schematic of the setup in Fig. S13). All flow rates were controlled by the mass flow controllers. For mixtures, gases were pre-mixed before contacting the membrane. The pressure of the feed side was controlled by adjusting a backpressure regulator. The transmembrane pressure difference was maintained at 1 bar. Argon was used as the sweep gas, carrying the permeate gas to a calibrated mass spectrometer (MS, Hiden Analytical, HPR-20) for the real-time analysis of the permeate concentration. The feed and sweep gas lines, and the membrane cell were heated in a convection oven to precisely control the temperature. The flow rate of the feed and sweep gas are 60 and 15 mL/min, respectively. The membrane module used in this study, based on 0.25 inch Swagelok VCR fitting has a good gas mixing. The high feed and permeate flow rate were used to minimize the concentration polarization. The area of the tested membrane is 1 mm^2. For testing the membrane performance stability undersaturated water conditions, the feed gas was bubbled through a water column at 25 °C. The permeate composition data was recorded and averaged after a steady-state condition was attained (typically 30 minutes after changing the conditions). The permeances, J_i, of gas i were calculated by equation (1):

$$J_i = X_i/(A \cdot \Delta P_i) \tag{1}$$

where X_i is the molar flow rate of component *i* across the membrane, A is the membrane area, and ΔP_i is the transmembrane pressure difference for the component *i*. The separation factor α_{ij} of the two components (*i* and *j*, where *i* is the faster-permeating component) was calculated by equation (2):

$$\alpha_{ij} = \left(C_i/C_j\right)_{permeate} / \left(C_i/C_j\right)_{feed} \tag{2}$$

where C_i is the concentration of component *i* in a given stream.

Supplementary Note I: **Facilitated transport membranes**

Although the facilitated transport (FT) membranes exhibit a very high CO_2/N_2 selectivity, in the range of 50-800, they require water in the feed as well as the permeate stream for the activation of the facilitated transport. As a result, the separation performance of FT membrane is extremely sensitive to the water content in membrane both on the feed side as well as the permeate side. Adding water to the permeate side increases the complexity and the energy-penalty of the separation because one would need to remove water from the purified CO_2 stream for subsequent sequestration or use. Water needs to be removed because (i) wet CO_2 pumping can lead to equipment corrosion, (ii) sequestering water alongside CO_2 is energy-inefficient and wasteful. Moreover, the performance of the facilitated transport membranes decreases after the transport carriers are saturated with CO_2.

Supplementary Note II: **Role of each component in SPONG membranes.**

The SPONG membrane is composed of atomically-thin nanoporous graphene matrix, and CO_2-selective polymeric chains supported onto the nanoporous matrix, making an ultrathin CO_2-selective membrane. The concept of the SPONG membrane relies on the synergistic properties of the individual components, ONG and polymers. One cannot use the individual component alone to realize a carbon capture performance. The nanopores in the ONG film are too large for molecular sieving and therefore, can only yield Knudsen selectivity. On the other hand, the low-molecular-weight polymer (PEI) and oligomer (PEGBA or PEGDE) cannot form a continuous, stable thin-film due to the mechanical stability issues.

The edges of graphene nanopores are composed of sp^3-hybridized carbon, which are functionalized with oxygen groups during the ozone treatment. The oxygen-functionalized edges can strongly interact with the functional polymers (PEI or PEGBA) by covalent bonding, hydrogen bonding and electrostatic interactions. As a result, the polymer layer on nanoporous graphene covers graphene nanopores, and therefore, effectively blocks the Knudsen diffusion of gases through the nanopores, and promotes the adsorbed-phase transport of CO_2.

It is predicted that the PEI or PEGBA-grafting can increase the adsorption of CO_2. Both PEI and PEG oligomers can preferentially interact with CO_2. The significant enhancement of adsorption by incorporating PEI and PEGDE is well documented in the literature.[5] For example, Huang et al reported that the adsorption capacity from the PEI-GO/ZIF-8 nanocomposite materials was six times higher than that of the pristine GO and ZIF-8, and the CO_2/N_2 adsorption selectivity was remarkably increased to 184.[6] The CO_2 adsorption capacity of PEI-modified TiO_2 particles was found much higher than that from TiO_2, and the incorporation of PEI-TiO_2 into PebaX membrane led to 193% enhancement of CO_2 permeability and 47% enhancement of CO_2/N_2 selectivity.[7] The incorporation of PEI-PEG-modified GO nanosheets (10 wt%) into PebaX membrane led to 2-times enhancement of solubility coefficient, while the Diffusion coefficient remained unchanged.[8]

It is noteworthy that swelling the PONG film with PEGDE oligomers can remarkably increase the CO_2 separation performance because of the improved sorption and free volume. The incorporation of PEGDE is expected to increase both the CO_2 solubility and diffusivity because the PEGDE has a high concentration of ethylene oxide units (95 wt%) and low crystallinity, offering high intrinsic free volume and CO2 solubility.[9,10] Jiang et al reported that the incorporation of 50 wt% of PEGDE into a crosslinked PEG matrix can increase the CO_2 solubility by 56%, and increase the CO_2 diffusivity by 3.7 times, resulting in 520% enhancement of CO_2 permeability.[9]

In the documented literature, at least 30-100 nm-thick polymer layer is needed to make a defect-free selective membrane.[11,12] Qiao and co-workers reported the preparation of 60 nm-thick CO_2-selective layer *via* atom transfer radical polymerization (ATRP) of PEG-based monomers on top of initiator-modified polydimethylsiloxane layer, which was precoated on a polyacrylonitrile support. [11] The *in situ* ATRP was used to enhance the density of PEG chains grafted on PDMS, thus facilitating the formation of defect-free ultrathin layer. In comparison, herein, a simple coating was utilized to introduce a much thinner polymer layer (10 nm), leading to ultrafast selective-transport of CO_2.

Supplementary Note III: **Analysis of the defect-density based on the Raman data.**

The evolution of the defect-density in graphene with the plasma exposure time can be divided into two stages: low-defect-density stage and high-defect-density stage. In the low-defect-density stage, the I_D/I_G increases with plasma exposure time due to that the breathing of six-atom ring in graphene lattice is activated by the presence of defects. In the high-defect-density stage, the I_D/I_G decreases with exposure time, attributing to the fact that the porosity of NG is increased with the time, reducing the number of ordered six-atom rings. In the low-defect-density stage, the average distance between defects, L_d, can be calculated according to the following equation[13,14]:

$$L_D^2(nm^2) = (1.8 \pm 0.5) \times 10^{-9}\, \lambda^4 (\tfrac{I_D}{I_G})^{-1} \quad \text{(S1)}$$

where λ is the Raman excitation wavelength (457 nm in this study).

In the high-defect-density stage, the L_d can be calculated according to the following correlation equation[13,14]:

$$\frac{I_D}{I_G} = D(\lambda) \times L_d^2 \quad \text{(S2)}$$

where $D(\lambda)$ can be obtained by imposing continuity between the two stages (~0.039 nm^{-2} in our study).

We can roughly estimate the defect density (number of defects per unit area), n_D, according to the following equation[14]:

$$n_D(cm^{-2}) = 10^{14}/(\pi L_d^2) \quad \text{(S3)}$$

In our case, the I_D/I_G maximized at 4 s of plasma time, indicating that after 4 s of plasma, the defects evolved into the high-defect-density stage. Thus, the defect density of as-synthesized graphene and 2 s plasma graphene can be calculated according to the equation S1 and S3, while the defect density of 4-8 s plasma graphene can be calculated according to the equation S2 and S3.

The increase in defect-density has contributions from i) increase in the pore-density resulting from continued nucleation of vacancy-defects, and ii) increase in the pore-size and therefore the edge-length, promoting the activation of D peak.

Supplementary Note IV: **Contamination-free transfer of NG to the TEM grid**

The conventional method to prepare suspended graphene specimen for TEM imaging is the well-known polymethyl methacrylate (PMMA) assisted wet-transfer approach. However, in this approach, PMMA residues are inevitably left behind, on top of the graphene lattice. Under the electron beam during the TEM imaging, the PMMA residues are mobile and can be trapped at the pore edges, resulting in the modification of the pores on graphene lattice.[15] In addition, due to the poor thermal conductivity of PMMA, the high-energy beam exposure leads to thermal decomposition of PMMA residues by local overheating, leading local rehybridization of carbons from sp^2

to sp^3.[16] As a result, these active sp^3 sites can nucleate new nanopores in graphene that further expand during beam exposure.[17] In comparison, the nanoporous carbon (NPC) film assisted method used in this work provides sufficient mechanical stability to transfer graphene to the TEM grid (Figure S3a) while completely avoiding unwanted contaminations on graphene's surface. The synthesis of NPC on graphene followed the protocol reported before with following modifications.[1] 0.1 g poly(styrene-b-4-vinyl pyridine) and 0.05 g turanose were used to make the precursor solution, and a pyrolysis temperature of 700 °C was used to obtain NPC film. The NPC film sitting on top of graphene was quite stable under the high-voltage electron beam (Supplementary Video). Since carbon is a good thermal conductor, the carbon film could rapidly transfer the beam-induced heat to the whole NPC/graphene sample preventing structural damage. Therefore, during the HRTEM imaging, the undesired pore modifications caused by polymer residues could be avoided in the NPC/graphene sample. We observed the movement of pore edges, but not pore-nucleation and pore-expansion, during TEM imaging (Supplementary Video). Moreover, a high density of open area allows an easy and extensive examination of the graphene surface (Figure S3b).

Supplementary Note V: **Thickness comparison between PONG and the SPONG films**

To reduce the error in thickness comparison between the PONG and the SPONG films because of the sample to sample variability, we cut a PONG film on copper in two pieces. While the first piece was transferred to a Si wafer without swelling (PONG specimen), the second piece was first swollen with PEGDE and then transferred to a Si wafer (SPONG specimen). Cross-sectional SEM images revealed thicknesses of 250 ± 10 nm and 260 ± 12 nm for the PEI-based PONG and the SPONG films, respectively, indicating that the thickness of the PEI-based PONG film increased by ca. 10 nm (100% swelling degree) after the swelling step (Fig. S11a and b). In the case of PEGBA-based PONG films, the thickness increase was lower than 10 nm (Figure S12).

Supplementary Note VI: **Discussion of the scale-up opportunity**

One of the key requirement for the scale-up is the possibility to produce membrane in a large area. It has been already demonstrated that the graphene film can be synthesized in a large area by the roll-to-roll production method.[18] Recent study demonstrated graphene membrane can be reinforced by carbon nanotube networks to fabricate membrane modules.[19]

The chemical treatment used here to synthesize ONG, using plasma and O_3 treatments, can be used in a scalable fashion. In this study, a complete polymer functionalization was achieved by spin-coating a thin layer of polymer, however, this can be replaced by a scalable spray-coating method. In future, low-cost porous polymer support can be used to support graphene films.[20,21] This is the first proof of concept of polymer functionalized membranes, and we believe that the permeance of such membrane can be increased further, reducing the membrane area needed for a certain separation. Few approaches to achieve this includes a) further increasing the porosity in graphene, while restricting the pore-size-distribution such that the maximum pore size is only a few nanometers, b) reducing the thickness of polymer layer, and c) using a CO_2-philic layer with higher permeability, for example, ionic liquids. Overall, this study is the proof-of-principle of the potential of this approach, and there is certainly a prospect in scaling up the polymer functionalized graphene membranes in the future.

Table S1. CO_2 permeance, CO_2/N_2 and CO_2/CH_4 ideal selectivity of PONG and SPONG membranes under single-gas permeation condition at 30 °C, 2 bar.

Membrane type	Mean pore size (nm)	Nomenclature	CO_2 permeance (GPU)	CO_2/N_2 ideal selectivity	CO_2/CH_4 ideal selectivity
PEI-based PONG	1.8	M14-PEI-4s	610	17.3	7.4
PEI-based SPONG	1.8	M3-PEI-4s	1000	42.3	17.9
PEI-based PONG	2.4	M15-PEI-6s	2030	15.3	7.8
PEI-based SPONG	2.4	M4-PEI-6s	5540	25.2	10.9
PEGBA-based PONG	1.8	M16-PEGBA-4s	320	23.5	12.8
PEGBA-based SPONG	1.8	M11-PEGBA-4s	630	57.2	20.5

Table S2. CO_2 permeance, CO_2/N_2 separation factor from the PEI- and PEGBA-based SPONG membranes under the mixed-gas feed conditions (CO_2/N_2 = 20/80 mol%) at 30 °C and 2 bar.

SPONG based on	Mean pore size (nm)	Nomenclature	CO_2 permeance (GPU)	CO_2/N_2 separation factor
PEI	1.8	M1-PEI-4s	980	41.1
PEI	1.8	M2-PEI-4s	920	38.8
PEI	2.4	M4-PEI-6s	5010	25.8
PEI	2.4	M5-PEI-6s	6110	21.4
PEI	2.4	M6-PEI-6s	4080	22.6
PEI	3.3	M8-PEI-8s	11080	15.2
PEI	3.3	M9-PEI-8s	8530	16.1
PEI	3.3	M10-PEI-8s	9500	17.5
PEGBA	3.3	M13-PEGBA-8s	4250	20.8

Table S3. CO_2 permeance, CO_2 permeability, CO_2/N_2 and CO_2/CH_4 ideal selectivity of the selective layer (SPONG films, no PTMSP), estimated from a resistance model[11] under single-gas permeation condition at 30 °C, 2 bar.

SPONG based on	Nomenclature	CO_2 permeance (GPU)	CO_2 permeability (Barrer)	CO_2/N_2 ideal selectivity	CO_2/CH_4 ideal selectivity
PEI	M4-PEI-6s	8670	173.4	33.7	15.1
PEI	M5-PEI-6s	10660	213.1	27.5	13.4
PEI	M6-PEI-6s	6270	124.1	30.7	12.7
PEI	M7-PEI-6s	4927	98.5	34.9	13.3

Note: The permeability of the selective layer is calculated based on a resistance model, as reported by Qiao and co-workers.[11] Briefly, the total resistance (R_T) of the membrane is the sum of the resistances from the PTMSP layer (R_{PL}), selective layer (R_{SL}), the porous support (R_S). R=T/P, where T is the film thickness, and P is the permeability. By assuming the R_S is zero, the total resistance can be expressed by the following equation:

$$R_T = R_{PL} + R_{SL} = \frac{T_{PL}}{P_{PL}} + \frac{T_{SL}}{P_{SL}}$$

where T_{PL} and T_{SL} are the thicknesses of PTMSP layer and selective layer, respectively, and P_{PL} and P_{SL} are the permeability of PTMSP layer and selective layer, respectively. R_T is determined by the membrane thickness and membrane permeability. T_{PL} and T_{SL} can be measured. Based on these data and the above equation, P_{SL} can be calculated. P_{PL} can be determined by measuring the gas permeance of the PTMSP membrane and its thickness. Here, a thin PTMSP membrane was prepared by spin coating. The permeability of CO_2, N_2, CH_4 were 3685, 361, 1084 Barrer, respectively. It is noteworthy that the permeability is much lower than the documented PTMSP membrane mainly because the PTMSP chains in the PTMSP film made by spin-coating stack more densely compared with that of PTMSP film made by evaporation-based solution-casting.[22] The CO_2 permeance, CO_2/N_2 and CO_2/CH_4 ideal selectivity can be calculated based on the P_{SL}.

Table S4. Comparison of the mixture separation performance of SPONG membranes with other typical composite and asymmetric membranes.

Membrane type	**Membrane descriptor**	**CO_2 permeability (Barrer)**	**CO_2 permeance (GPU)**	**CO_2/N_2 selectivity**	**CO_2/CH_4 selectivity**	**Reference**
Commercial membrane	Cellulose acetate	-	110	30		23
Graphene oxide (GO)	GO with PEGBA	20	186.3	59.4	66.8	24
	GO with ionic-liquid	0.6	37	130	40	25
	GO	-	103	18	10	26
Facilitated transport membranes	GO	-	110	52	28	26
	Borate in GO	5	650	57	75	27
	Piperazine in GO	16	1020	680		28
	Enzymatic solution	47	2600	788		29
	Polyvinylamine	1520	1827	500		30
Mixed matrix membranes	UiO-66-NH_2 in PEBAX®	500	338	57	20	31
	ZIF-8 in PEBAX®	518	345	31.7	13	32
	CuBDC nanosheets in PIM-1	267	407		15.6	33
	GO in thermally-reduced (TR) polymer	62	1784	17.7*	32.4*	34
	Carbon nanotubes in cellulose acetate	-	741.7	40.2		35
	ZIF-8 in Ultem®	-	26	36		36
Polymeric membranes	Polyethylene glycol (PEG) /Polydimethylsiloxane (PDMS)	158	1260	43*		11
	PEG/PDMS	151	1210	22		11
	PEG/NH_2-MIL-53	90	3000	34*		12
	PEG/NH_2-MIL-53	78	2600	14		12
	DAmPEG-TMC	183	1310	33		37
	Pebax2533/PEG-*b*-PPFPA	1860	3330	22*		38
	Polaris™	-	1000	50		23
	TR polymer	2907	1938	13*	14*	39
	Poly(ionic liquids)	349	132	27		40
SPONG membranes	M1-PEI-4s	20	980	41.1		This work
	M2-PEI-4s	18	920	38.8		
	M4-PEI-6s	100	5010	25.8		
	M4-PEI-6s	111	5540	25.2*	10.9*	
	M5-PEI-6s	122	6110	21.4		
	M6-PEI-6s	82	4080	22.6		
	M8-PEI-8s	222	11080	15.2		
	M9-PEI-8s	171	8530	16.1		
	M10-PEI-8s	190	9500	17.5		
	M13-PEGBA-8s	85	4250	20.8		

* Indicate the ideal selectivity.

GO: graphene oxide; PEGBA: poly(ethylene glycol)-bis-amine; CuBDC: copper 1,4-benzene dicarboxylate based MOF; PIM: polymer with intrinsic microporosity; DAmPEG-TMC: diaminopolyethylene glycol-trimesoyl chloride; PEG-b-PPFPA: poly(ethylene glycol)-block poly(pentafluoropropyl actylate).

Table S5. Comparison of pore density, obtained from the analysis of HRTEM images, with defect density obtained from the Raman spectroscopy.

Plasma exposure time / s	Pore density[§] [× 10^{12} cm^{-2}]	Defect density[#] [× 10^{12} cm^{-2}]
4	2.1	0.7
6	2.3	0.9
8	-	1.2

[§] The pore density is obtained from the analysis of the HRTEM images. Specifically, the pore density = pore number/graphene area, where *graphene area* is the survey area, and *pore number* is the amount of pores found in the survey area.

[#] The defect density is obtained from the Raman analysis. The specific calculation can be found in Supplementary Note III.

Table S6. Percentage of C, N and O atoms in ONG, and PEI- and PEGBA-functionalized ONG. Calculations based on the XPS data. The polymer functionalization was carried out by exposing ONG to dilute polymer solution followed by rinsing in water to remove excess polymer.

Film type	C1s (%)	N1s (%)	O1s (%)
ONG	75.4	0.0	23.9
PEI-functionalized ONG	72.4	8.8	18.9
PEGBA-functionalized ONG	74.7	1.9	23.4

Table S7. The concentration of C-N+C-O, C-C (sp^2 and sp^3), and C=O in ONG, and PEI- and PEGBA-functionalized ONG. Calculations based on the XPS data. The polymer functionalization was carried out by exposing ONG to dilute polymer solution followed by rinsing in water to remove excess polymer.

Film type	**C-N+C-O**	**C-C (sp^2)**	**C-C (sp^3)**	**C=O**
ONG	7.4	82.0	6.7	4.0
PEI-functionalized ONG	37.1	47.6	9.4	6.0
PEGBA-functionalized ONG	26.5	56.8	11.5	5.3

Table S8. The binding energy (BE) and the BE distance between C-N/C-O and N1s in PEI-, PEGBA-based PONG, and PEI reference film.

Film type	**BE (eV)**		**BE Distance between C-N/C-O and N1s (eV)**
	C-N/C-O	**N1s**	
PEI-functionalized ONG	285.6	399.6	114.1
PEGBA-functionalized ONG	285.7	399.5	113.8
PEI reference film	285.5	399.0	113.5

Note: In comparison to the absolute BE of the N1s line, the BE distance between C-N/C-O and N1s, independent from the BE calibration, was calculated. The BE distance between C-N/C-O and N1s indicates the relative N1s BE of PEI- or PEGBA-functionalized ONG compared with the corresponding BE from C-N/C-O, from which one can calculate the BE shift ruling out the influence of BE calibration. The PEI-functionalized ONG still exhibits a chemical shift of 0.6 eV, verifying the chemical binding between PEI and ONG. It well-documented that PEI can rapidly react with oxidized graphene through a facile ring-opening reaction between the amino and epoxy groups at room temperature[41–44]. Here, it is very likely that the chemical binding between PEI and ONG was formed by the ring-opening reaction, resulting in covalent bonds between nitrogen from PEI and carbon from graphene.

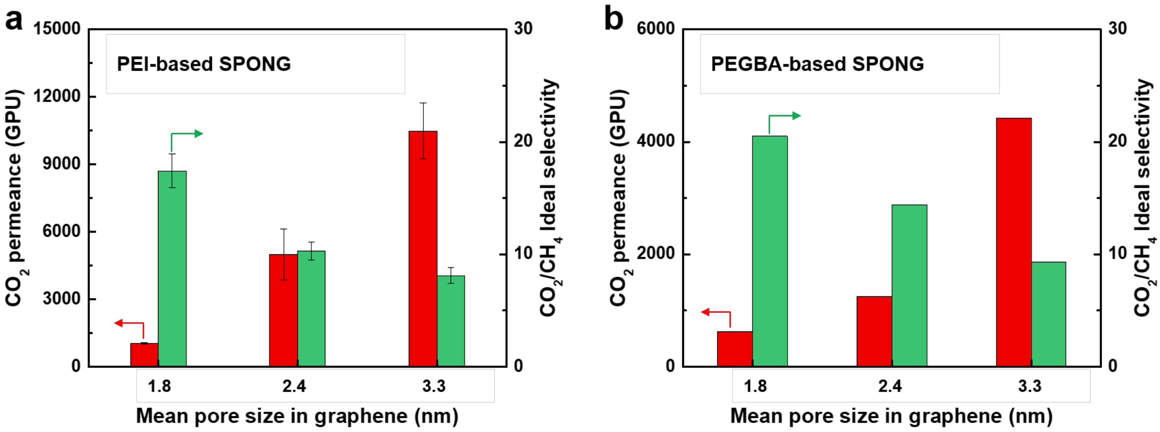

Figure S1. CO_2/CH_4 separation performance from (**a**) PEI-based SPONG membranes, and (**b**) PEGBA-based SPONG membranes.

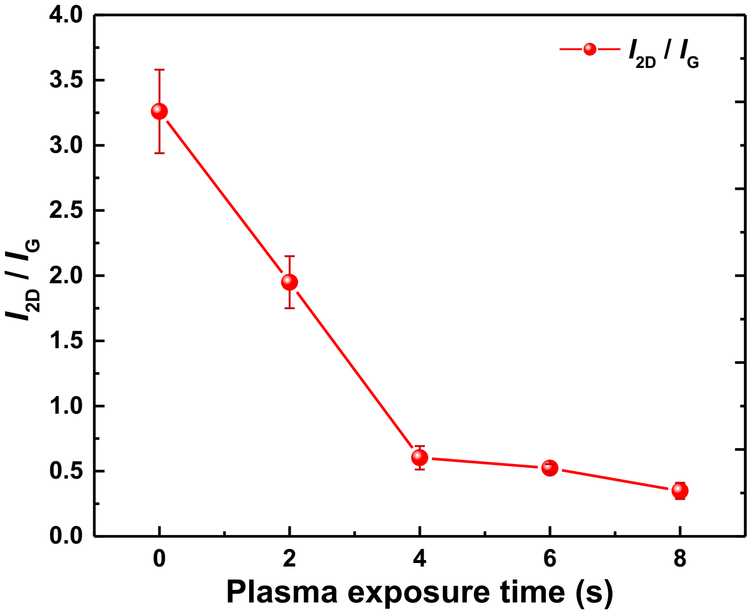

Figure S2. **Plot of I_{2D}/I_G as a function of plasma exposure time.** The decrease in I_{2D}/I_G ratio with the plasma exposure time indicates increasing defects in graphene.[13]

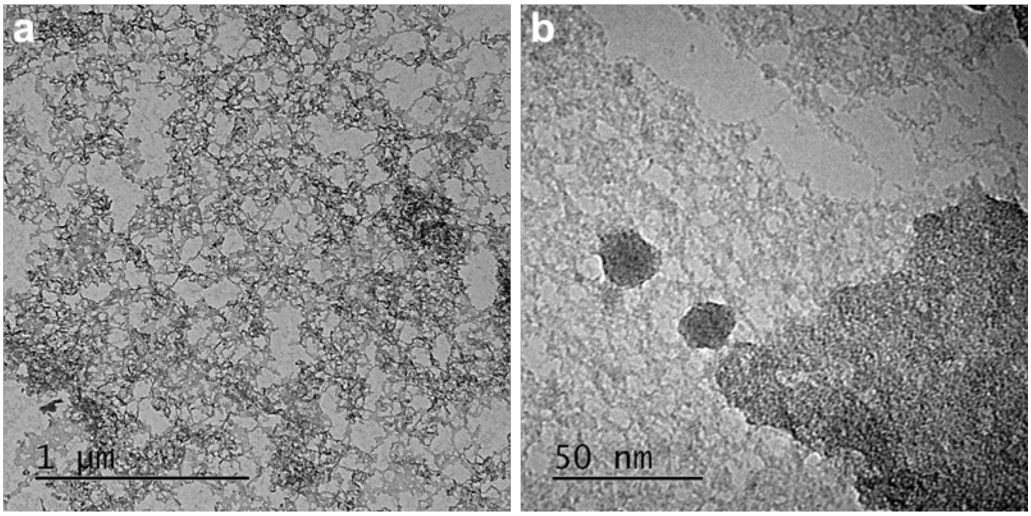

Figure S3. **TEM images of graphene covered with the NPC film**. **a**) Interconnected carbon structure gives sufficient mechanical stability to graphene during transfer to the TEM grid. **b**) The high-density of carbon-free area yield a significant portion of graphene available for HRTEM.

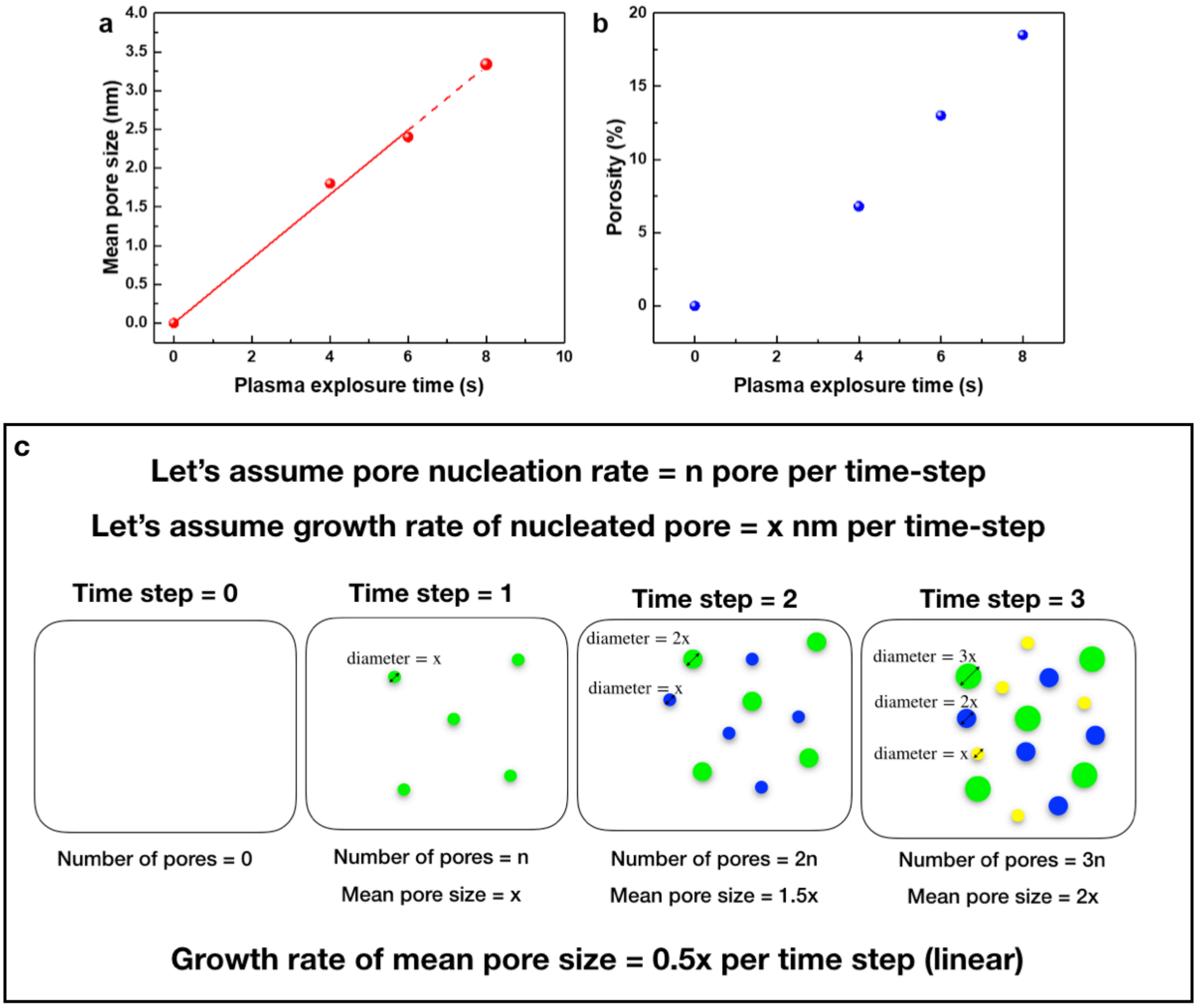

Let's assume pore nucleation rate = n pore per time-step

Let's assume growth rate of nucleated pore = x nm per time-step

Number of pores = 0

Number of pores = n
Mean pore size = x

Number of pores = 2n
Mean pore size = 1.5x

Number of pores = 3n
Mean pore size = 2x

Growth rate of mean pore size = 0.5x per time step (linear)

Figure S4. Increase in the mean pore size (a) and porosity (b) as a function of the plasma time. The mean pore size is observed to increase at a linear rate with etching time. An explanation for this is provided in (c). The mean pore size and the corresponding porosity of the graphene etched for 8 s was extrapolated.

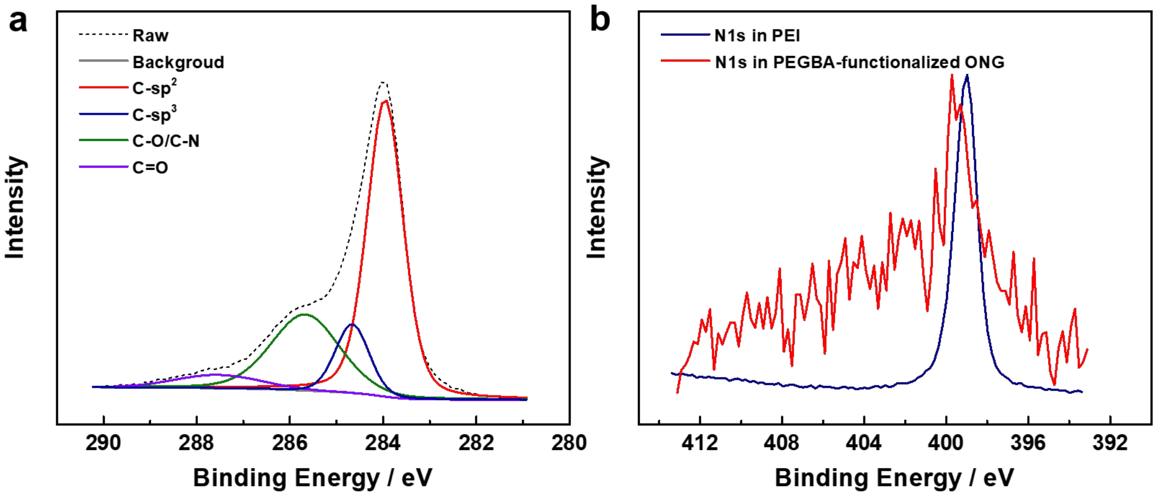

Figure S5. **XPS characterization of PEGBA functionalized ONG. a**) XPS spectrum of PEGBA-functionalized ONG. **b**) Comparison of the N1s peaks from the PEGBA-functionalized ONG and a PEI reference film. The XPS spectra from the PEGBA functionalized ONG revealed higher C1s peaks at 284.7 and 285.7 eV (Table S7 and S8), essentially from the sp^3-hybridized C-C and C-N group of PEGBA, indicating a successful functionalization of ONG with PEGBA.

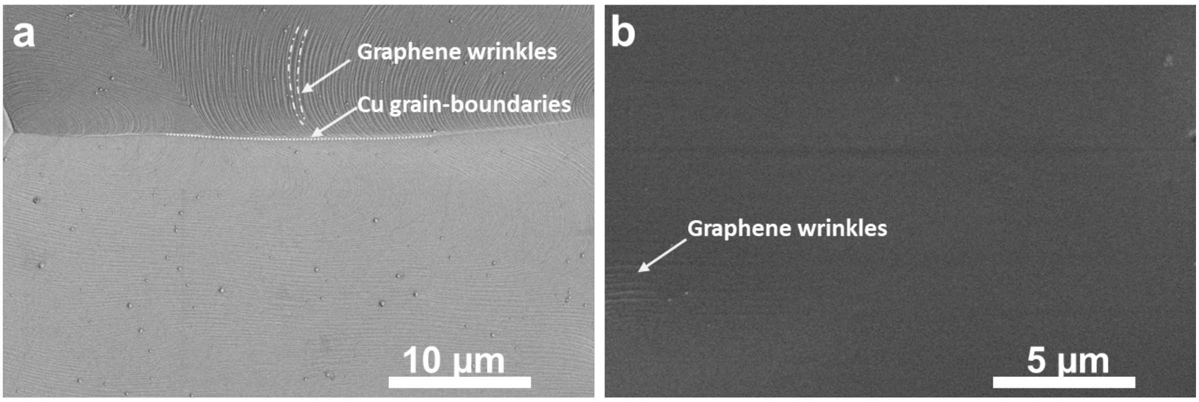

Figure S6. **Surface morphology of the graphene films observed by SEM. a)** The as-synthesized CVD graphene on copper foil. Typical copper grain boundaries and graphene wrinkles are clearly present. **b)** PEI-based PONG. The graphene wrinkles are still present but become less distinct compared with that of graphene/Cu sample, indicating that the PEI film is very thin.

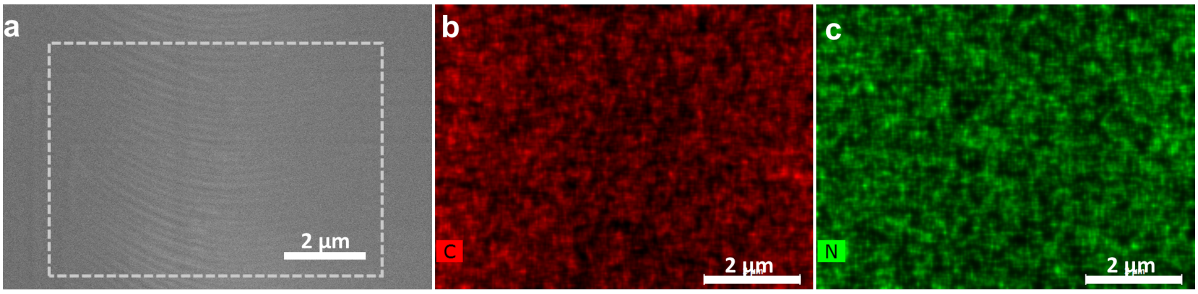

Figure S7. **Characterization of the morphology of the PEI-based PONG film**. **a**) A uniform surface of the film as revealed by SEM. The graphene wrinkles are visible attributing to the fact that the thickness of PEI film is only a few nanometers. **b-c)** The element distribution probed by EDS mapping for carbon (**b**), and for nitrogen (**c**), revealing a uniform coverage of the thin polymer film. The white rectangle in (a) shows the scanned area for the EDS mapping.

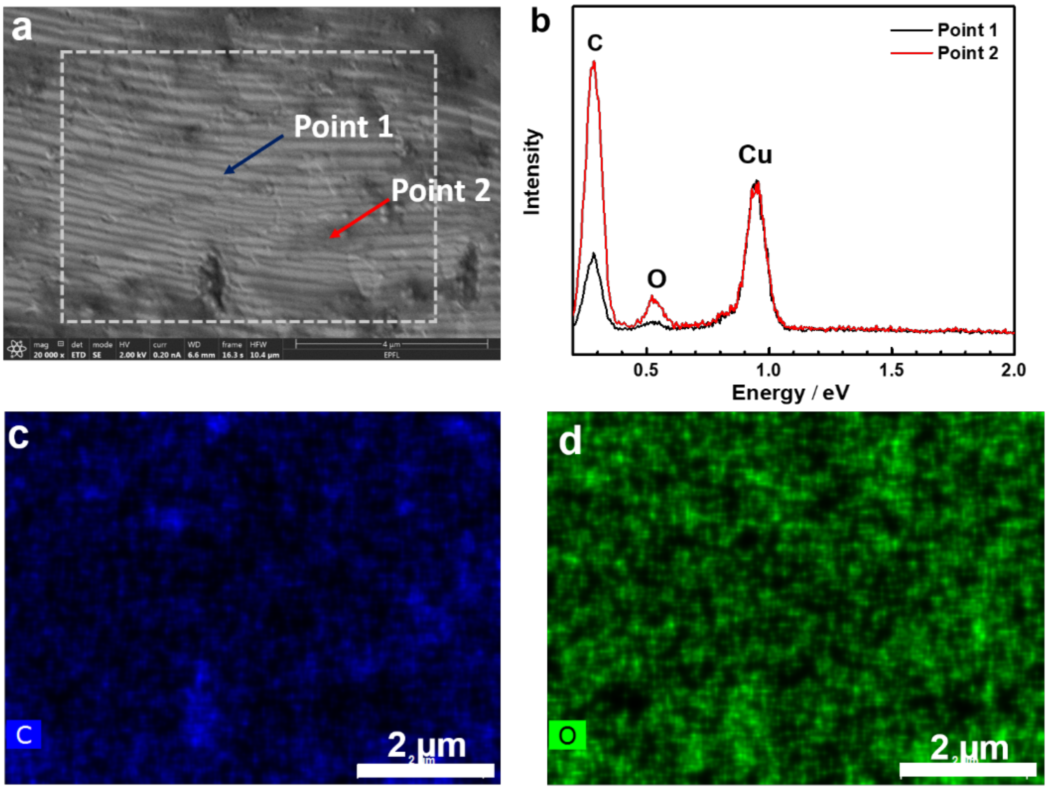

Figure S8. **Characterization of the morphology of PEGBA-based PONG film. a**) SEM image of surface morphology of PONG film sitting on Cu. **b)** EDS analysis of points 1 and 2. **c-d)** The element distribution probed by EDS mapping for carbon (c), and oxygen (d). The white rectangle in (a) shows the scanned area for the EDS mapping. The EDS analysis and element distribution demonstrate that although the PEGBA distribution on graphene is not uniform, the PEGBA polymer still fully covers the graphene surface.

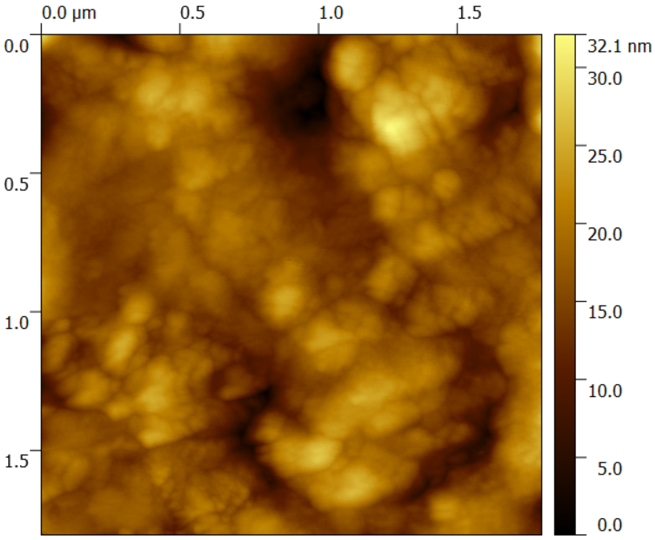

Figure S9. **AFM topography image of the PEGBA-based PONG film**.

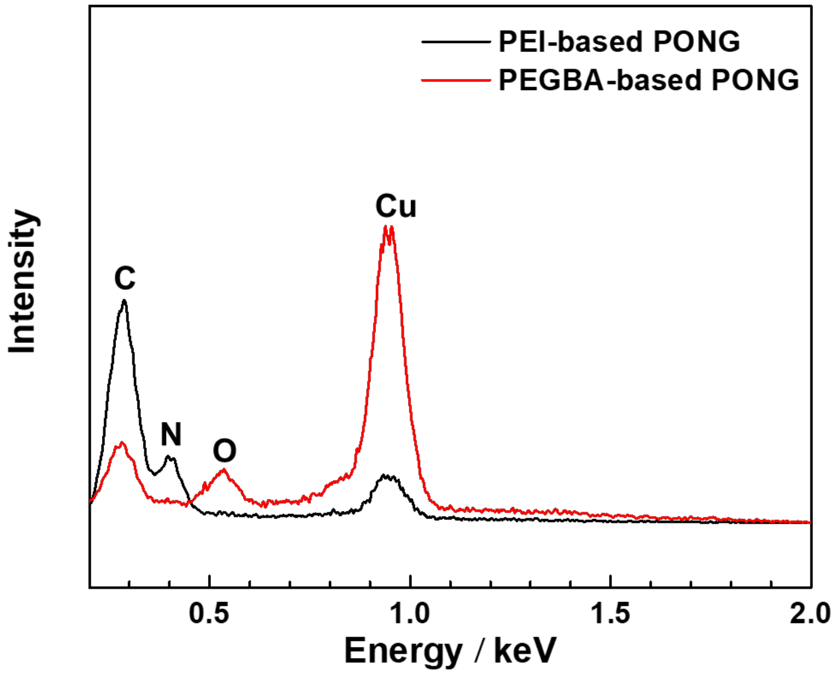

Figure S10. **A comparison of the EDS from the PONG films based on PEI and PEGBA**. The PEI-based film is predominantly comprised of C and N, whereas the PEGBA-based film is mainly comprised of C and O. The N from the terminal amine group of PEGBA is not detected because its concentration is only 2.8 wt%. The intensity of the underlying Cu is much stronger for the PEGBA-based PONG indicating that the PEGBA film is thinner than the PEI film.

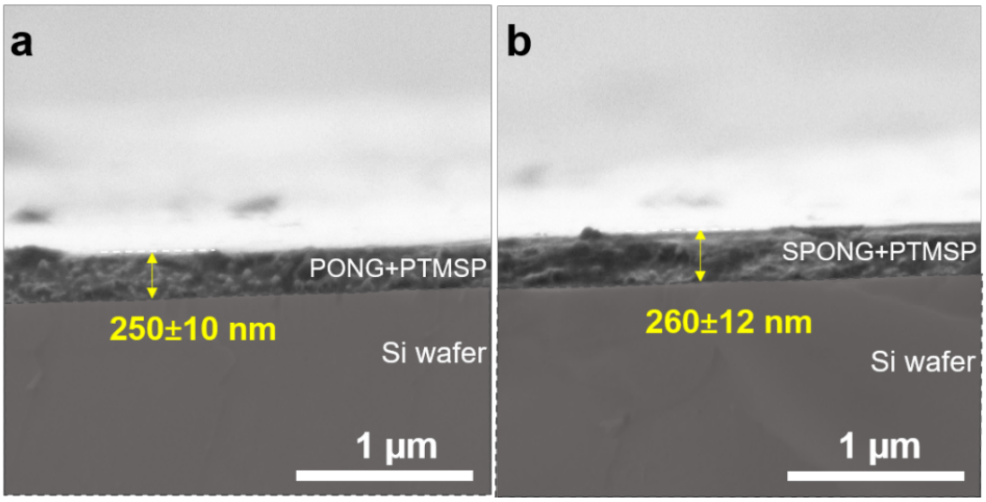

Figure S11. **Cross-sectional SEM images of the PEI based** (**a**) PONG and (**b**) SPONG film mechanically reinforced with a top layer of a PTMSP film.

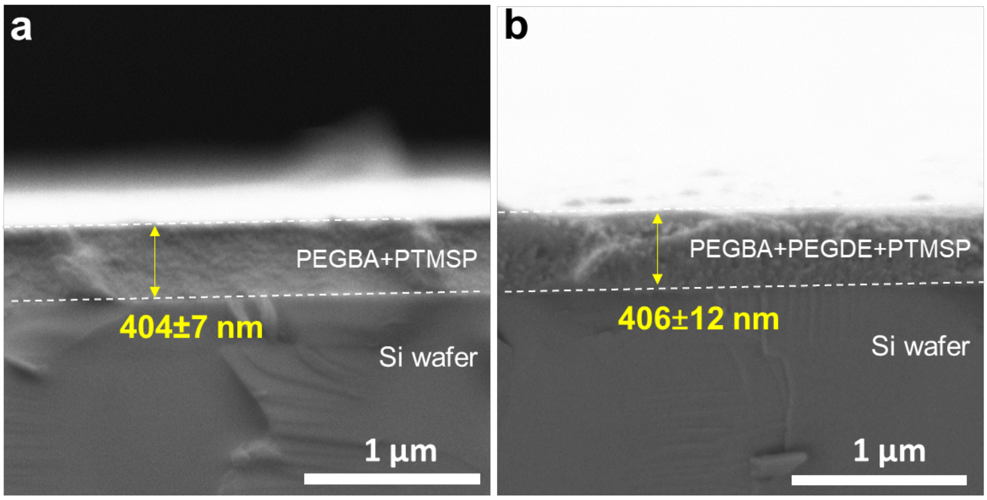

Figure S12. **Cross-sectional SEM images revealing thickness of the PEGBA-based PONG and SPONG films mechanically reinforced with a top layer of PTMSP film** (**a**) PONG (**b**) SPONG. The films were transferred to Si wafer to facilitate the preparation of the cross-section. We note that the PTMSP layer on PEI based PONG film was thinner, ca. 250 nm, which can be attributed to the weaker interaction between the PEI and the PTMSP, which was dissolved in toluene.

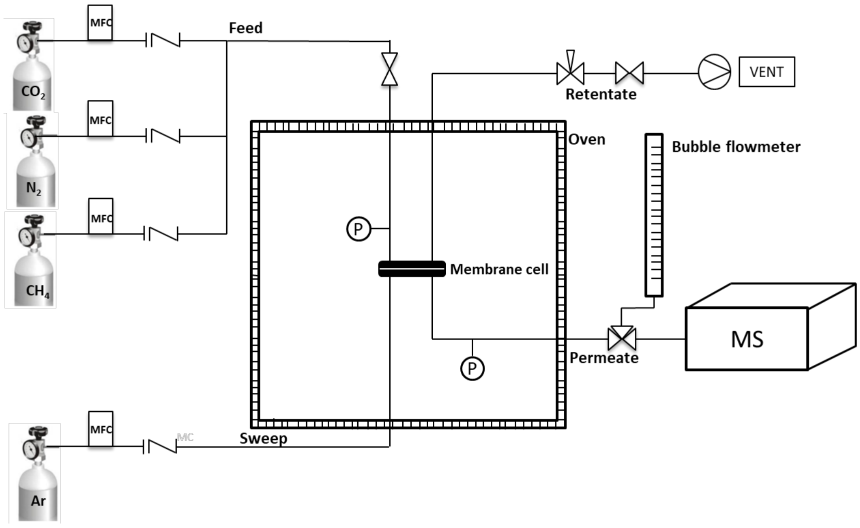

Figure S13. Schematic of the gas permeance setup.

References

1 S. Huang, M. Dakhchoune, W. Luo, E. Oveisi, G. He, M. Rezaei, J. Zhao, D. T. L. Alexander, A. Züttel and M. S. Strano, *Nat. Commun.*, 2018, **9**, 2632.

2 X. Li, W. Cai, J. An, S. Kim, J. Nah, D. Yang, R. Piner, A. Velamakanni, I. Jung and E. Tutuc, *Science*, 2009, **324**, 1312–1314.

3 A. J. Strudwick, N. E. Weber, M. G. Schwab, M. Kettner, R. T. Weitz, J. R. Wünsch, K. Müllen and H. Sachdev, *ACS Nano*, 2015, **9**, 31–42.

4 X. Li, Y. Zhu, W. Cai, M. Borysiak, B. Han, D. Chen, R. D. Piner, L. Colombo and R. S. Ruoff, *Nano Lett.*, 2009, **9**, 4359–4363.

5 Z. Qiao, S. Zhao, M. Sheng, J. Wang, S. Wang, Z. Wang, C. Zhong and M. D. Guiver, *Nat. Mater.*, 2018, **18**, 163.

6 A. Huang and B. Feng, *Int. J. Hydrogen Energy*, 2018, **43**, 2224–2231.

7 H. Zhu, J. Yuan, J. Zhao, G. Liu and W. Jin, *Sep. Purif. Technol.*, 2019, **214**, 78–86.

8 X. Li, Y. Cheng, H. Zhang, S. Wang, Z. Jiang, R. Guo and H. Wu, *ACS Appl. Mater. Interfaces*, 2015, **7**, 5528–5537.

9 X. Jiang, S. Li and L. Shao, *Energy Environ. Sci.*, 2017, **10**, 1339–1344.

10 S. Wang, Y. Liu, S. Huang, H. Wu, Y. Li, Z. Tian and Z. Jiang, *J. Memb. Sci.*, 2014, **460**, 62–70.

11 Q. Fu, J. Kim, P. A. Gurr, J. M. P. Scofield, S. E. Kentish and G. G. Qiao, *Energy Environ. Sci.*, 2016, **9**, 434–440.

12 K. Xie, Q. Fu, C. Xu, H. Lu, Q. Zhao, R. Curtain, D. Gu, P. A. Webley and G. G. Qiao, *Energy Environ. Sci.*, 2018, **11**, 544–550.

13 A. C. Ferrari and D. M. Basko, *Nat. Nanotechnol.*, 2013, **8**, 235–246.

14 L. G. Cançado, A. Jorio, E. H. M. Ferreira, F. Stavale, C. A. Achete, R. B. Capaz, M. V. O. Moutinho, A. Lombardo, T. S. Kulmala and A. C. Ferrari, *Nano Lett.*, 2011, **11**, 3190–3196.

15 J. C. Meyer, C. O. Girit, M. F. Crommie and A. Zettl, *Nature*, 2008, **454**, 319.

16 Y. C. Lin, C. C. Lu, C. H. Yeh, C. Jin, K. Suenaga and P. W. Chiu, *Nano Lett.*, 2012, **12**, 414–419.

17 W. Yuan, Y. Zhou, Y. Li, C. Li, H. Peng, J. Zhang, Z. Liu, L. Dai and G. Shi, *Sci. Rep.*, 2013, **3**, 2248.

18 S. Bae, H. Kim, Y. Lee, X. Xu, J.-S. Park, Y. Zheng, J. Balakrishnan, T. Lei, H. R. Kim and Y. Il Song, *Nat. Nanotechnol.*, 2010, **5**, 574.

19 Y. Yang, X. Yang, L. Liang, Y. Gao, H. Cheng, X. Li, M. Zou, R. Ma, Q. Yuan and X. Duan, *Science*, 2019, **364**, 1057–1062.

20 P. R. Kidambi, D. D. Mariappan, N. T. Dee, A. Vyatskikh, S. Zhang, R. Karnik and A. J. Hart, *ACS Appl. Mater. Interfaces*, 2018, **10**, 10369–10378.

21 L. Prozorovska and P. R. Kidambi, *Adv. Mater.*, 2018, **1801179**, 1–24.

22 D. Gomes, S. P. Nunes and K.-V. Peinemann, *J. Memb. Sci.*, 2005, **246**, 13–25.

23 T. C. Merkel, H. Lin, X. Wei and R. Baker, *J. Memb. Sci.*, 2010, **359**, 126–139.

24 S. Wang, Y. Xie, G. He, Q. Xin, J. Zhang, L. Yang, Y. Li, H. Wu, Y. Zhang, M. D. Guiver and Z. Jiang, *Angew. Chem. Int. Ed.*, 2017, **56**, 14246–14251.

25 M. Karunakaran, L. F. Villalobos, M. Kumar, R. Shevate, F. H. Akhtar and K.-V. Peinemann, *J. Mater. Chem. A*, 2017, **5**, 649–656.

26 H. W. Kim, H. W. Yoon, S.-M. Yoon, B. M. Yoo, B. K. Ahn, Y. H. Cho, H. J. Shin, H. Yang, U. Paik and S. Kwon, *Science*, 2013, **342**, 91–95.

27 S. Wang, Y. Wu, N. Zhang, G. He, Q. Xin, X. Wu, H. Wu, X. Cao, M. D. Guiver and Z. Jiang, *Energy Environ. Sci.*, 2016, **9**, 3107–3112.

28 F. Zhou, H. N. Tien, W. L. Xu, J. T. Chen, Q. Liu, E. Hicks, M. Fathizadeh, S. Li and M. Yu, *Nat. Commun.*, 2017, **8**, 2107.

29 Y. Fu, Y.-B. Jiang, D. Dunphy, H. Xiong, E. Coker, S. Chou, H. Zhang, J. M. Vanegas, J. G. Croissant and J. L. Cecchi, *Nat. Commun.*, 2018, **9**, 990.

30 T.-J. Kim, H. Vrålstad, M. Sandru and M.-B. Hägg, *J. Memb. Sci.*, 2013, **428**, 218–224.

31 P. D. Sutrisna, J. Hou, M. Y. Zulkifli, H. Li, Y. Zhang, W. Liang, D. M. D'Alessandro and V. Chen, *J. Mater. Chem. A*, 2018, **6**, 918–931.

32 P. D. Sutrisna, J. Hou, H. Li, Y. Zhang and V. Chen, *J. Memb. Sci.*, 2017, **524**, 266–279.

33 Y. Cheng, X. Wang, C. Jia, Y. Wang, L. Zhai, Q. Wang and D. Zhao, *J. Memb. Sci.*, 2017, **539**, 213–223.

34 S. Kim, J. Hou, Y. Wang, R. Ou, G. P. Simon, J. G. Seong, Y. M. Lee and H. Wang, *J. Mater. Chem. A*, 2018, **6**, 7668–7674.

35 A. L. Ahmad, Z. A. Jawad, S. C. Low and S. H. S. Zein, *J. Memb. Sci.*, 2014, **451**, 55–66.

36 Y. Dai, J. R. Johnson, O. Karvan, D. S. Sholl and W. J. Koros, *J. Memb. Sci.*, 2012, **401–402**, 76–82.

37 S. Li, Z. Wang, C. Zhang, M. Wang, F. Yuan, J. Wang and S. Wang, *J. Memb. Sci.*, 2013, **436**, 121–131.

38 J. M. P. Scofield, P. A. Gurr, J. Kim, Q. Fu, S. E. Kentish and G. G. Qiao, *J. Memb. Sci.*, 2016, **499**, 191–200.

39 S. Kim, S. H. Han and Y. M. Lee, *J. Memb. Sci.*, 2012, **403–404**, 169–178.

40 D. Nikolaeva, I. Azcune, E. Sheridan, M. Sandru, A. Genua, M. Tanczyk, M. Jaschik, K. Warmuzinski, J. C. Jansen and I. F. J. Vankelecom, *J. Mater. Chem. A*, 2017, **5**, 19808–19818.
41 X. Z. Tang, C. Mu, W. Zhu, X. Yan, X. Hu and J. Yang, *Carbon N. Y.*, 2016, **98**, 432–440.
42 M. Wang, X. Duan, Y. Xu and X. Duan, *ACS Nano*, 2016, **10**, 7231–7247.
43 J. Zou and F. Kim, *Nat. Commun.*, 2014, **5**, 1–9.
44 Z. Fan, K. Hiu Laam Po, K. Kit Wong, S. Chen and S. Ping Lau, *Acs Appl. Nano Mater.*, 2018, **1**, 1811–1818.